

Supporting Information

Sacrificial Interlayer for Promoting Charge Transport in Hematite Photoanode

Kai Zhang,^{†,§} Tianjiao Dong,^{†,‡,§} Guancai Xie,^{†,‡,§} Liming Guan,^{†,§} Beidou Guo,^{†,§} Qin Xiang,^{†,‡} Yawen Dai,^{†,‡} Liangqiu Tian,^{†,‡} Aisha Batool,^{†,‡} Saad Ullah Jan,^{†,‡} Rajender Boddula,^{†,‡} Akbar Ali Thebo,^{†,‡} and Jian Ru Gong^{*,†}

[†]Chinese Academy of Sciences (CAS) Center for Excellence in Nanoscience, CAS Key Laboratory of Nanosystem and Hierarchy Fabrication, National Center for Nanoscience and Technology, Beijing 100190, P. R. China

[‡]University of Chinese Academy of Sciences, Beijing 100049, P. R. China

Corresponding Author.

^{*}E-mail address: gongjr@nanoctr.cn (Prof. J. R. Gong)

Author Contributions.

[§]These authors contributed equally.

Index

Figure S1. Top-view and cross-sectional SEM images of β -FeOOH and 0.5% volume fraction TiCl_4 ethanol solution coated β -FeOOH ($\text{TiCl}_4@ \beta$ -FeOOH) thin films.

Figure S2. XRD patterns of β -FeOOH and 0.5% volume fraction TiCl_4 ethanol solution coated β -FeOOH ($\text{TiCl}_4@ \beta$ -FeOOH) thin films.

Figure S3. Feature size distribution of α - Fe_2O_3 , 0.5%- $\text{TiO}_2@ \text{Ti}:\alpha$ - Fe_2O_3 , and $\text{Ti}:\alpha$ - Fe_2O_3 photoanodes.

Figure S4. Ti 2p XPS spectra of α - Fe_2O_3 and x- $\text{TiO}_2@ \text{Ti}:\alpha$ - Fe_2O_3 photoanodes.

Table S1. The surface chemical compositions, the positions of Ti 2p_{3/2} XPS peaks, the physical surface areas, the flat-band potentials of the prepared photoanodes and their calculated donor concentrations.

Figure S5. The Mott-Schottky plots of the α - Fe_2O_3 , x- $\text{TiO}_2@ \text{Ti}:\alpha$ - Fe_2O_3 ($x = 0.25\%$, 0.5%, 1.0%, and 1.5%), and $\text{Ti}:\alpha$ - Fe_2O_3 photoanodes.

Figure S6. Physical surface area measurements. (a) The standard absorbance-concentration curve of Orange II. (b) The absorbance of the desorbed Orange II solutions of the α - Fe_2O_3 , 0.5%- $\text{TiO}_2@ \text{Ti}:\alpha$ - Fe_2O_3 , and $\text{Ti}:\alpha$ - Fe_2O_3 photoanodes.

Figure S7. UV-vis transmittance, reflectance, and absorbance of α - Fe_2O_3 and x- $\text{TiO}_2@ \text{Ti}:\alpha$ - Fe_2O_3 photoanodes.

Figure S8. The photocurrent onset potentials of α - Fe_2O_3 , 0.5%- $\text{TiO}_2@ \text{Ti}:\alpha$ - Fe_2O_3 , and $\text{Ti}:\alpha$ - Fe_2O_3 photoanodes.

Figure S9. The $J-V$ curves of α - Fe_2O_3 , 0.5%- $\text{TiO}_2@ \text{Ti}:\alpha$ - Fe_2O_3 and $\text{Ti}:\alpha$ - Fe_2O_3 photoanodes under chopped light illumination.

Figure S10. Open circuit potential measurements of α - Fe_2O_3 , 0.5%- $\text{TiO}_2@ \text{Ti}:\alpha$ - Fe_2O_3 , and $\text{Ti}:\alpha$ - Fe_2O_3 photoanodes under illumination (red square) and in dark (black square) conditions.

Figure S11. The valance band spectra of α - Fe_2O_3 , 0.5%- $\text{TiO}_2@ \text{Ti}:\alpha$ - Fe_2O_3 and $\text{Ti}:\alpha$ - Fe_2O_3 photoanodes.

Figure S12. Ti 2p XPS spectra of α - Fe_2O_3 , 0.5%- $\text{TiO}_2@ \text{Ti}:\alpha$ - Fe_2O_3 and $\text{Ti}:\alpha$ - Fe_2O_3 photoanodes.

Figure S13. UV-vis transmittance, reflectance, and absorbance of 0.5%- $\text{TiO}_2@ \text{Ti}:\alpha$ - Fe_2O_3 and $\text{Ti}:\alpha$ - Fe_2O_3 photoanodes.

Figure S14. The variation in the PEC performance of the 0.5%- $\text{TiO}_2@ \text{Ti}:\alpha$ - Fe_2O_3 , 1.0%- $\text{TiO}_2@ \text{Ti}:\alpha$ - Fe_2O_3 , and α - Fe_2O_3 photoanodes with increasing H_2O_2 soaking time.

Figure S15. SEM images of the α - Fe_2O_3 photoanodes at different H_2O_2 soaking times.

Table S2. Comparison of PEC performance of $\text{Ti}:\alpha$ - Fe_2O_3 photoanodes.

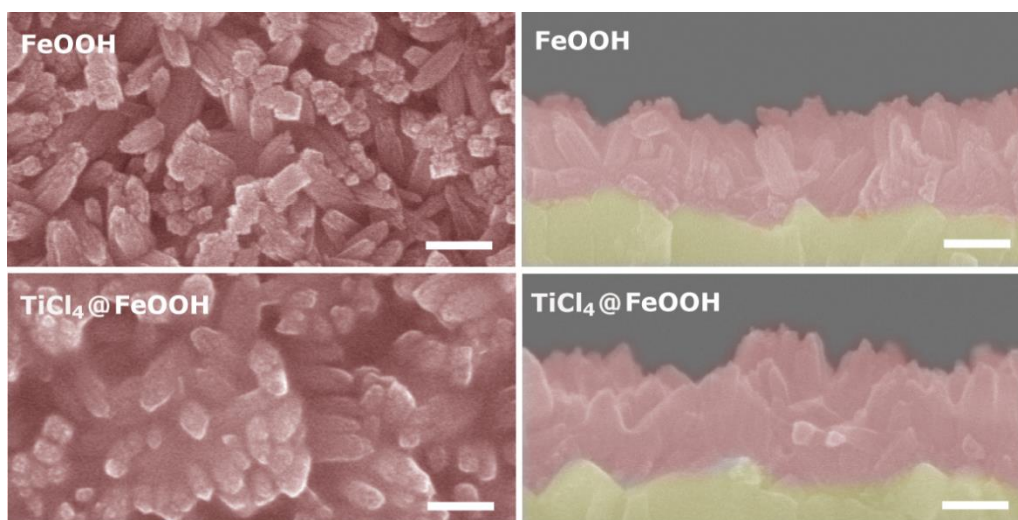


Figure S1. Top-view and cross-sectional SEM images of β -FeOOH and TiCl_4 (0.5% volume fraction) ethanol solution coated β -FeOOH ($\text{TiCl}_4@ \beta$ -FeOOH) thin films. Scale bars: 100 nm.

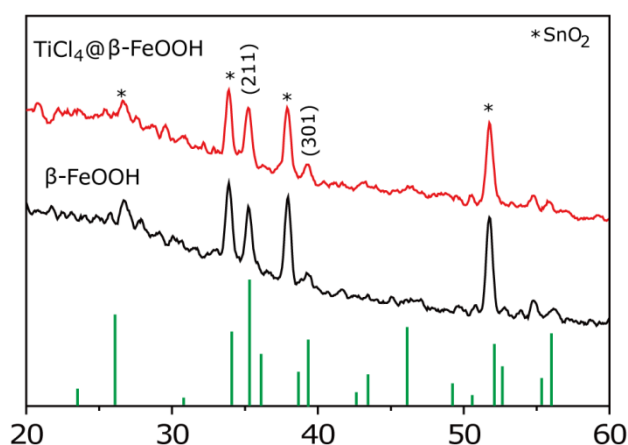


Figure S2. XRD patterns of β -FeOOH and TiCl_4 (0.5% volume fraction) ethanol solution coated β -FeOOH ($\text{TiCl}_4@ \beta$ -FeOOH) thin films. The green lines highlight the akaganeite crystal structure (PDF Card No. 34-1266).

β -FeOOH nanorods self-assembled into bundles of about 40 nm in diameter are uniformly grown on the FTO substrate (SEM images in the first row of Figure S1), and the intense diffraction peak at 35.2° in its XRD pattern (The black pattern in Figure S2) can be indexed to the (211) plane of the akaganeite crystal structure, implying the strong preferential orientation of the [211] direction vertical to the FTO substrate. After spin-coating 0.5% volume fraction TiCl_4 ethanol solution, a thin and uniform coating

layer through which one can see the well-preserved nanorod morphology of β -FeOOH, is evident from its SEM top-view image (The second row in Figure S1), and the akaganeite crystal structure of β -FeOOH is also well-retained according to its similar XRD pattern (The red pattern in Figure S2) to that of the β -FeOOH thin film.

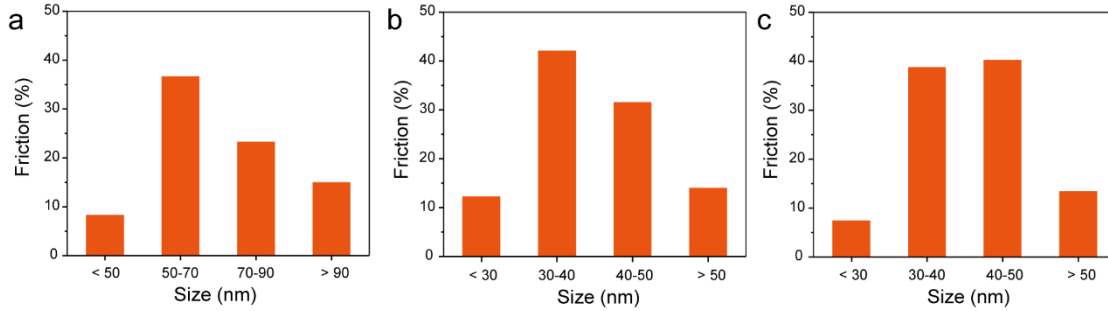


Figure S3. Feature size distribution of (a) α -Fe₂O₃, (b) 0.5%-TiO₂@Ti: α -Fe₂O₃, and (c) Ti: α -Fe₂O₃ photoanodes.

The statistical feature size distribution of hematite nanostructures in the α -Fe₂O₃, 0.5%-TiO₂@Ti: α -Fe₂O₃, and Ti: α -Fe₂O₃ was conducted by analyzing at least 50 rodlike nanostructures from SEM images. It is obvious that the feature size is mostly around 30-50 nm for the 0.5%-TiO₂@Ti: α -Fe₂O₃ photoanode, which is much smaller than that of the α -Fe₂O₃ photoanode (50-90 nm), while the feature size is also about 30-50 nm for the Ti: α -Fe₂O₃ photoanode.

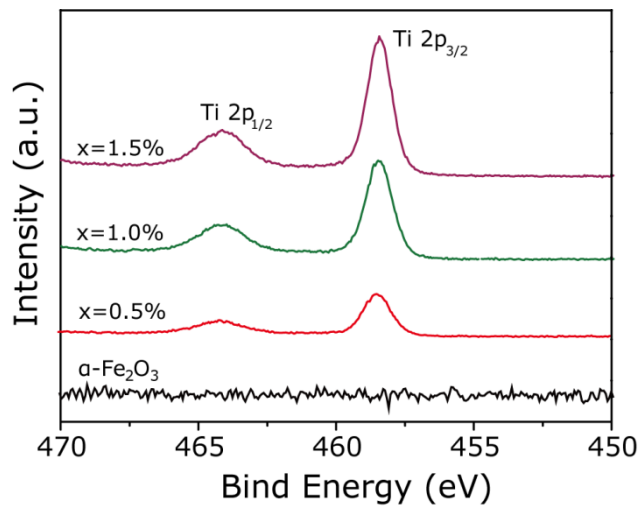


Figure S4. Ti 2p XPS spectra of α -Fe₂O₃ and x-TiO₂@Ti: α -Fe₂O₃ (x=0.5%, 1.0%, and 1.5%) photoanodes.

Table S1. The surface chemical composition, the position of Ti 2p_{3/2} XPS peaks, the physical surface area, the flat-band potential of the prepared photoanodes and their calculated donor concentrations

Sample	Surface chemical concentration (%)				Ti 2p _{3/2} XPS peak position (eV)	Physical surface area (cm ²)	Flat-band potential (V vs. RHE)	N _d ×10 ¹⁶ (cm ⁻³)
	Ti	Fe	O	C				
α -Fe ₂ O ₃	0	17.9	49.0	30.7	-	10.23	0.75	0.68
0.5%-TiO ₂ @Ti: α -Fe ₂ O	10.5	10.2	53.9	24.5	458.46	13.23	0.76	1.86
1.0%-TiO ₂ @Ti: α -Fe ₂ O	11.9	5.4	49.6	30.6	458.49	-	0.77	-
1.5%-TiO ₂ @Ti: α -Fe ₂ O	14.7	4.4	49.1	29.5	458.47	-	0.80	-
Ti: α -Fe ₂ O ₃	3.2	14.1	52.4	29.6	458.50	14.30	0.76	1.66

Intensive Ti 2p XPS peaks can be found in all of the x -TiO₂@Ti: α -Fe₂O₃ (x = 0.5%, 1.0%, and 1.5%) photoanodes (Figure S4). Owing to the spin-orbit coupling effect, all the Ti 2p peaks give rise to a doublet with the two states having different binding energies. The two spin-orbit peaks (2p_{1/2}:2p_{3/2}) have specific area ratios of 1:2 based on the degeneracy of each spin state, and is also constrained to a peak separation of 6.17 eV.¹ The binding energy of Ti 2p_{3/2} peaks are all approximate to that of the Ti 2p_{3/2} peak in TiO₂ (458.5 eV), and the calculated surface concentrations of Ti from XPS analysis are all comparable to or even much higher than that of Fe at the surface of these photoanodes (Figure S4 and Table S1). Based on the above analysis together with the appearance of TiO₂ XRD diffraction peaks in the photoanodes spin-coated with high TiCl₄ concentration ethanol solutions before annealing (Figure 1b), one can confirm the existence of TiO₂ on the surface of the x -TiO₂@Ti: α -Fe₂O₃ photoanodes.

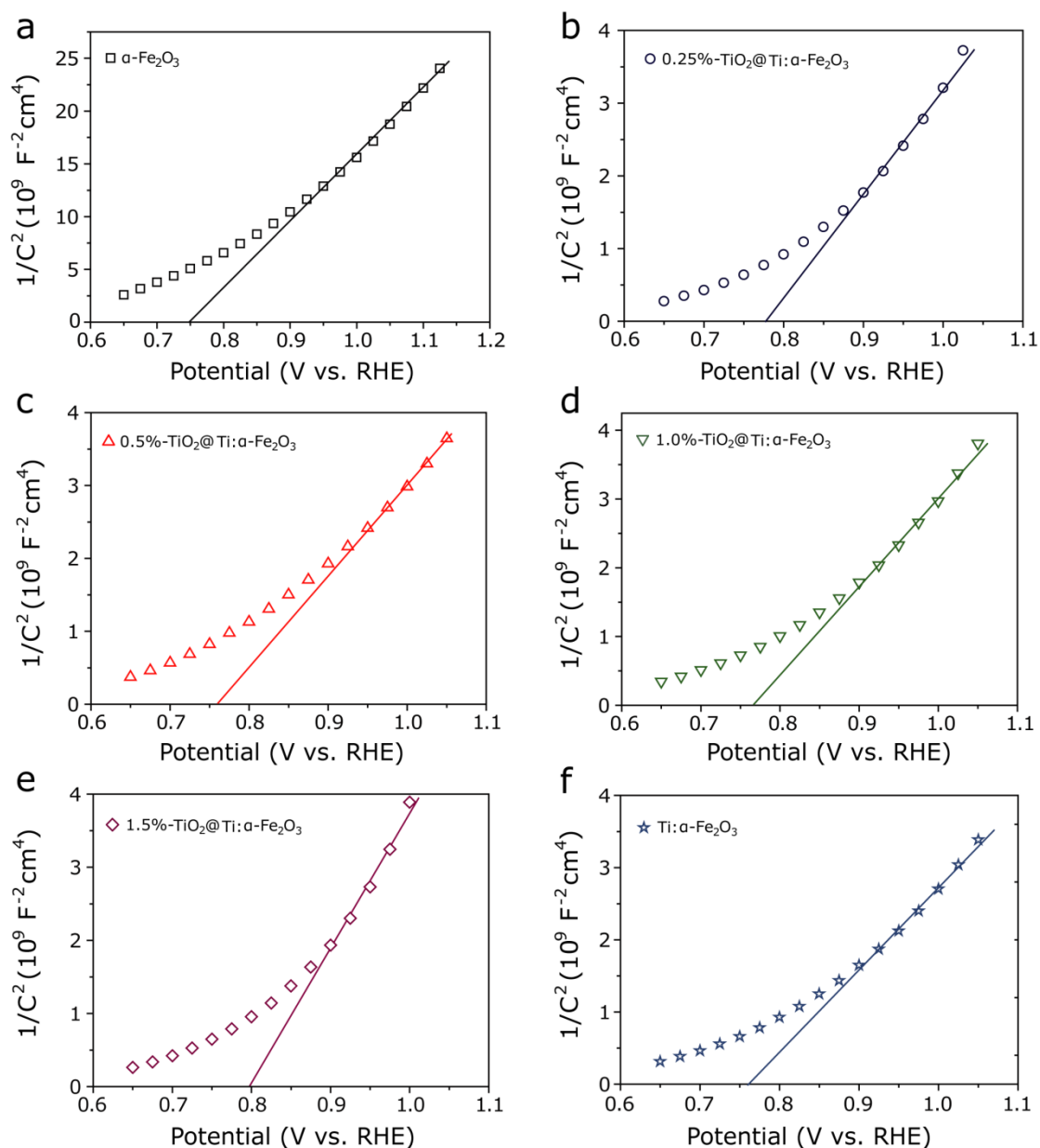


Figure S5. The Mott–Schottky plots of the (a) α -Fe₂O₃, (b) 0.25%-TiO₂@Ti: α -Fe₂O₃, (c) 0.5%-TiO₂@Ti: α -Fe₂O₃, (d) 1.0%-TiO₂@Ti: α -Fe₂O₃, (e) 1.5%-TiO₂@Ti: α -Fe₂O₃, and (f) Ti: α -Fe₂O₃ photoanodes.

The n-type conductive nature of all the prepared photoanodes is evident from the positive slopes of the Mott–Schottky curves in Figure S5, and the slopes of the Mott–Schottky curves of all the x -TiO₂@Ti: α -Fe₂O₃ photoanodes are much smaller than that of the α -Fe₂O₃ photoanode, indicating the increase in the donor concentration after Ti doping.

The spin-coating of TiCl_4 ethanol solution causes a little (≤ 50 mV) change in the flat-band potentials of the $x\text{-TiO}_2@\text{Ti}:\alpha\text{-Fe}_2\text{O}_3$ photoanodes compared with that of the $\alpha\text{-Fe}_2\text{O}_3$ photoanode (Table S1).

The flat-band potential remains the same in the 0.5%- $\text{TiO}_2@\text{Ti}:\alpha\text{-Fe}_2\text{O}_3$ and $\text{Ti}:\alpha\text{-Fe}_2\text{O}_3$ photoanodes (Table S1), indicating that the H_2O_2 soaking treatment has no effect on the Fermi level of the photoanode.

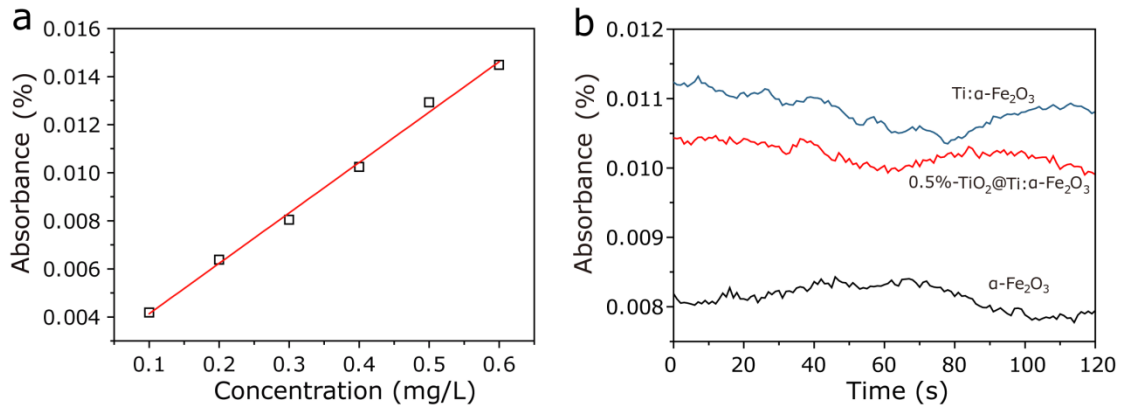


Figure S6. Physical surface area measurements. (a) The standard absorbance-concentration curve of Orange II. (b) The absorbance of the desorbed Orange II solutions of the $\alpha\text{-Fe}_2\text{O}_3$, 0.5%- $\text{TiO}_2@\text{Ti}:\alpha\text{-Fe}_2\text{O}_3$, and $\text{Ti}:\alpha\text{-Fe}_2\text{O}_3$ photoanodes.

The physical surface areas in Table S1 were calculated by the Orange II absorption quantities of the $\alpha\text{-Fe}_2\text{O}_3$, 0.5%- $\text{TiO}_2@\text{Ti}:\alpha\text{-Fe}_2\text{O}_3$, and $\text{Ti}:\alpha\text{-Fe}_2\text{O}_3$ photoanodes according to references.²⁻³ It can be calculated by using the following equation:

$$S = N_A s_0 \frac{(A - b) \times V}{kM} \quad (1)$$

here, N_A is the Avogadro constant, s_0 is the area occupied by an Orange II molecule (0.40 nm^2), A and V are the absorbance and volume of the Orange II solution, k and b are the slope and intercept derived from the standard absorbance-concentration curve in Figure S6a, and M is the mole weight of Orange II.

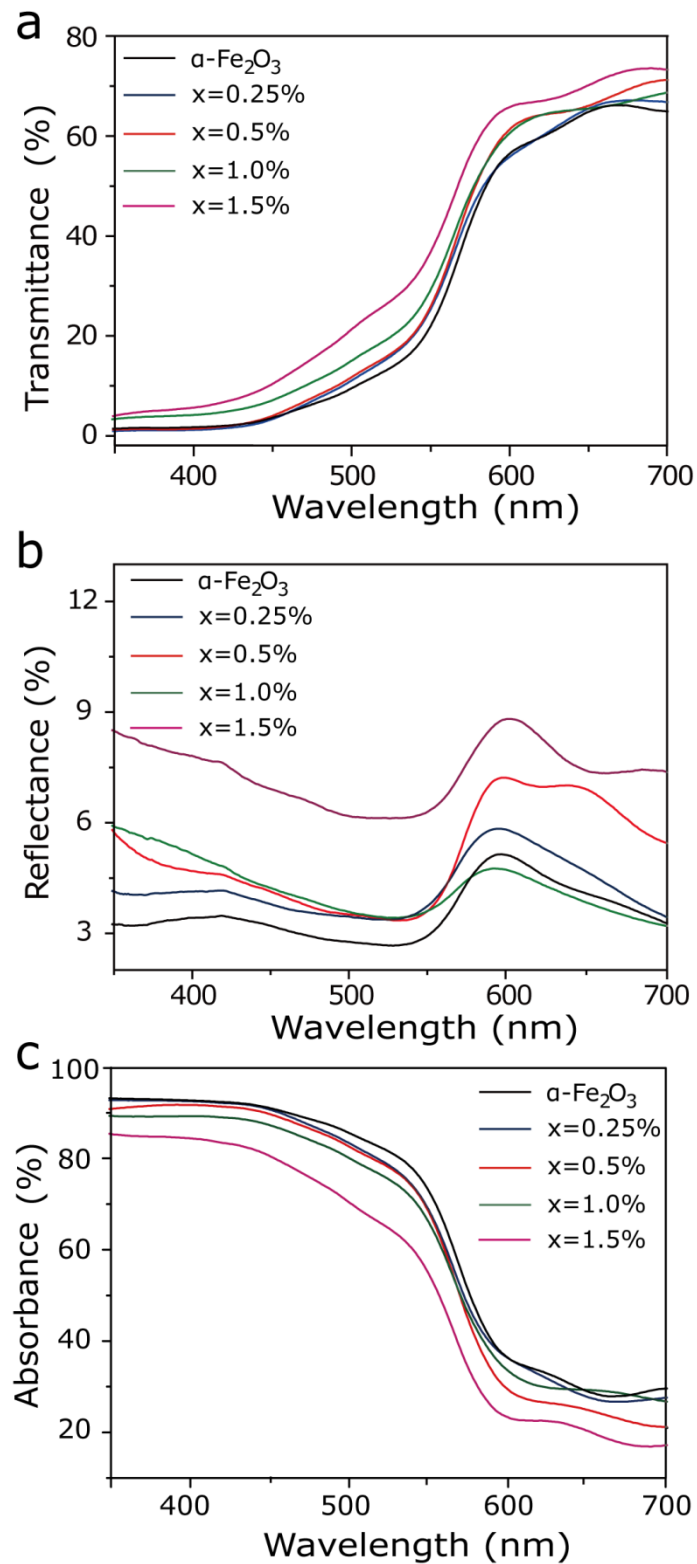


Figure S7. UV–vis transmittance (a), reflectance (b), and absorbance (c) of $\alpha\text{-Fe}_2\text{O}_3$ and $x\text{-TiO}_2@\text{Ti}:\alpha\text{-Fe}_2\text{O}_3$ ($x=0.25\%$, 0.5% , 1.0% , and 1.5%) photoanodes.

The absorbance (A) (Figure S7c) was calculated with the formula $A=1 - T - R$, where T is the total transmittance (Figure S7a), and R is the total reflectance (Figure S7b). The UV-vis absorbance of all of the x -TiO₂@Ti: α -Fe₂O₃ photoanodes ($x=0.25\%$, 0.5% , 1.0% and 1.5%) are lower than that of the α -Fe₂O₃ photoanode. Thus, the contribution of light absorption to the improved PEC activity can be excluded.

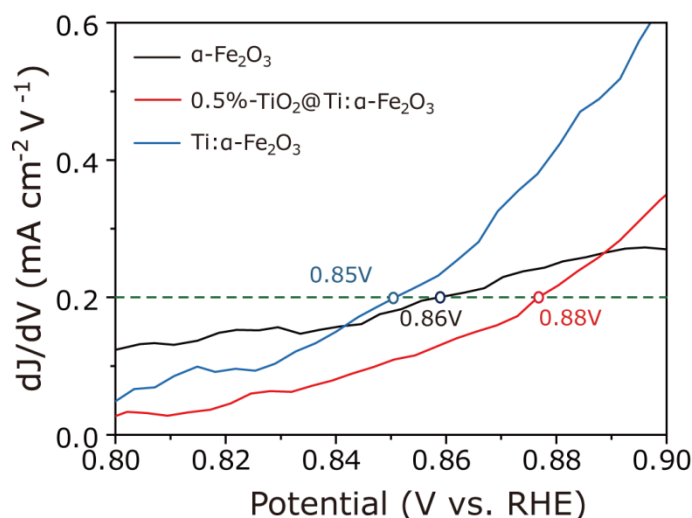


Figure S8. The photocurrent onset potentials of α -Fe₂O₃, 0.5%-TiO₂@Ti: α -Fe₂O₃ and Ti: α -Fe₂O₃ photoanodes derived from Figure 3a.

The photocurrent onset potential was defined as the potential where the first-order derivative of the photocurrent density as a function of the applied potential (dJ/dV) reaches a value of $0.20 \text{ mA cm}^{-2} \text{ V}^{-1}$.⁴ The photocurrent onset potentials for α -Fe₂O₃ and 0.5%-TiO₂@Ti: α -Fe₂O₃ photoanodes are 0.86 V and 0.88 V vs. RHE, respectively. That is, in comparison with that of the α -Fe₂O₃ photoanode, an anodic shift of 20 mV can be found in the photocurrent onset potential of the 0.5%-TiO₂@Ti: α -Fe₂O₃ photoanode.

The photocurrent onset potential for the Ti: α -Fe₂O₃ photoanode is 0.85 V vs. RHE, indicating that there is a cathodic shift of around 30 mV in the photocurrent onset potential compared with that of the 0.5%-TiO₂@Ti: α -Fe₂O₃ photoanode. This is also slightly better than that of the α -Fe₂O₃ photoanode.

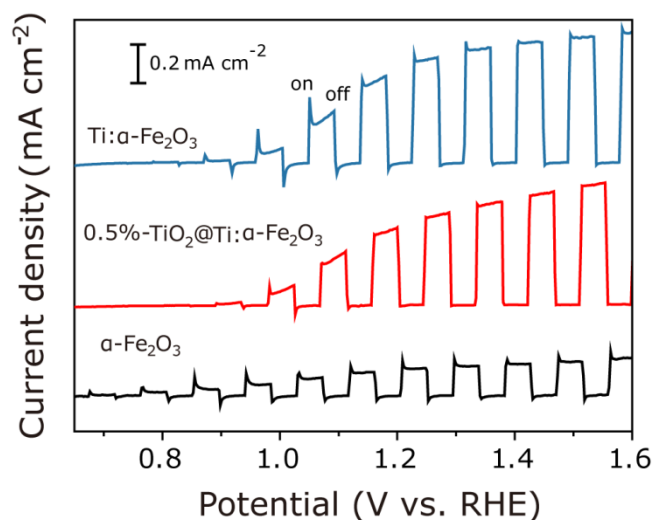


Figure S9. The J – V curves of α -Fe₂O₃, 0.5%-TiO₂@Ti: α -Fe₂O₃ and Ti: α -Fe₂O₃ photoanodes under chopped light illumination.

We measured the J – V curves under chopped light illumination (light chopped J – V curves) to qualitatively probe the surface charge recombination in the α -Fe₂O₃, 0.5%-TiO₂@Ti: α -Fe₂O₃ and Ti: α -Fe₂O₃ photoanodes. As shown in Figure S9, both anodic and cathodic transient peaks exist in the light chopped J – V curve of the α -Fe₂O₃ photoanode, indicating the severe surface charge recombination in this sample.⁵⁻⁶ By contrast, the transient current spikes completely disappear in the light chopped J – V curve of the 0.5%-TiO₂@Ti: α -Fe₂O₃ photoanode, implying the suppression of the surface charge recombination by TiO₂ on its surface.

After H₂O₂ treatment, we see that the transient current peaks reappear in the Ti: α -Fe₂O₃ photoanode, which should be attributed to the removal of the surface TiO₂ encapsulation layer.

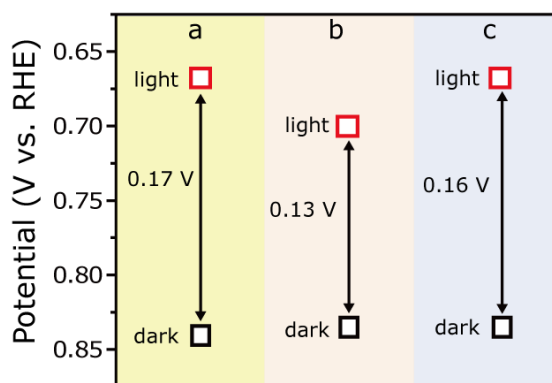


Figure S10. Open circuit potential measurements of (a) α -Fe₂O₃, (b) 0.5%-TiO₂@Ti: α -Fe₂O₃, and (c) Ti: α -Fe₂O₃ photoanodes under illumination (red square) and in dark (black square) conditions.

Open circuit potential measurements have been conducted on α -Fe₂O₃, 0.5%-TiO₂@Ti: α -Fe₂O₃, and Ti: α -Fe₂O₃ photoanodes under illumination (red square) and in dark (black square) conditions. The photovoltages generated in α -Fe₂O₃, 0.5%-TiO₂@Ti: α -Fe₂O₃, and Ti: α -Fe₂O₃ photoanodes are 170, 130, and 160 mV, respectively.

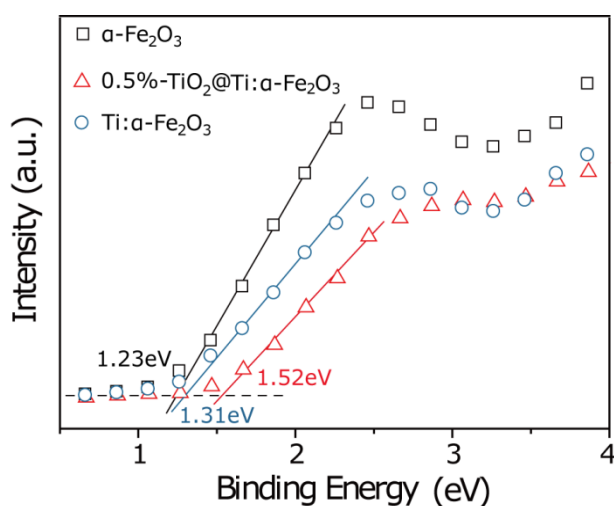


Figure S11. XPS valence band spectra of α -Fe₂O₃, 0.5%-TiO₂@Ti: α -Fe₂O₃, and Ti: α -Fe₂O₃ photoanodes.

The valence band maximum (VBM) of the 0.5%-TiO₂@Ti:α-Fe₂O₃ photoanode (1.52 eV below the Fermi level) is located more positively than that of the α-Fe₂O₃ photoanode (1.23 eV below the Fermi level).

The VBM of Ti:α-Fe₂O₃ photoanode (1.31 eV below Fermi level) shifts about 210 meV negatively to in comparison with that of the 0.5%-TiO₂@Ti:α-Fe₂O₃ photoanode (1.52 eV below the Fermi level).

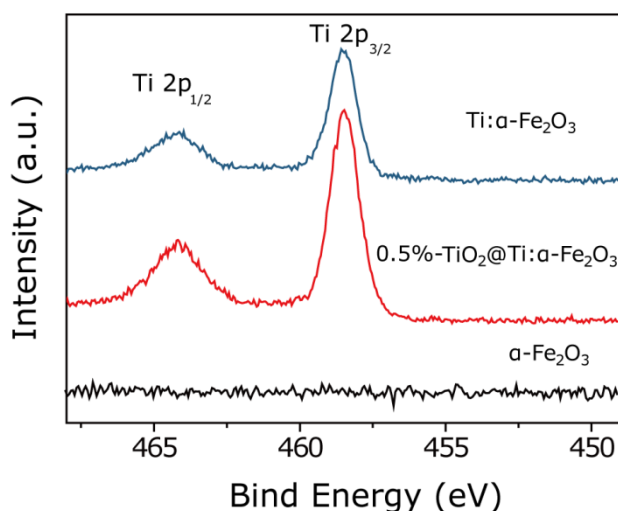


Figure S12. Ti 2p XPS spectra of α-Fe₂O₃, 0.5%-TiO₂@Ti:α-Fe₂O₃, and Ti:α-Fe₂O₃ photoanodes.

There is a 30% decrease in the intensity of the Ti 2p XPS peak after H₂O₂ soaking treatment, indicating the reduction in the concentration of Ti on the surface of the Ti:α-Fe₂O₃ photoanode.

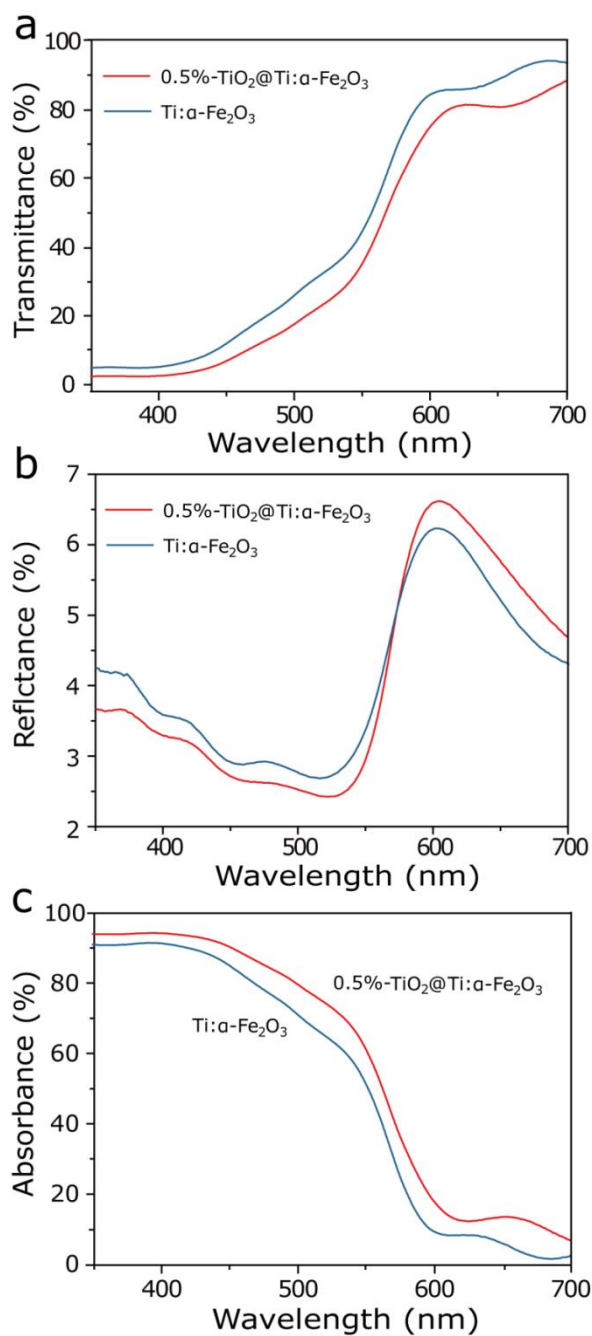


Figure S13. UV–vis (a) transmittance, (b) reflectance, and (c) absorbance of 0.5%-TiO₂@Ti:α-Fe₂O₃ and Ti:α-Fe₂O₃ photoanodes.

The absorbance (A) (Figure S13c) was calculated with the formula $A=1 - T - R$, where T is the total transmittance (Figure S13a) and R is the total reflectance (Figure S13b). The UV-vis absorbance of the Ti:α-Fe₂O₃ photoanode is a little lower than that of the 0.5%-TiO₂@Ti:α-Fe₂O₃ photoanode because of the decrease in the thickness of the photoanode after removal of the surface TiO₂.

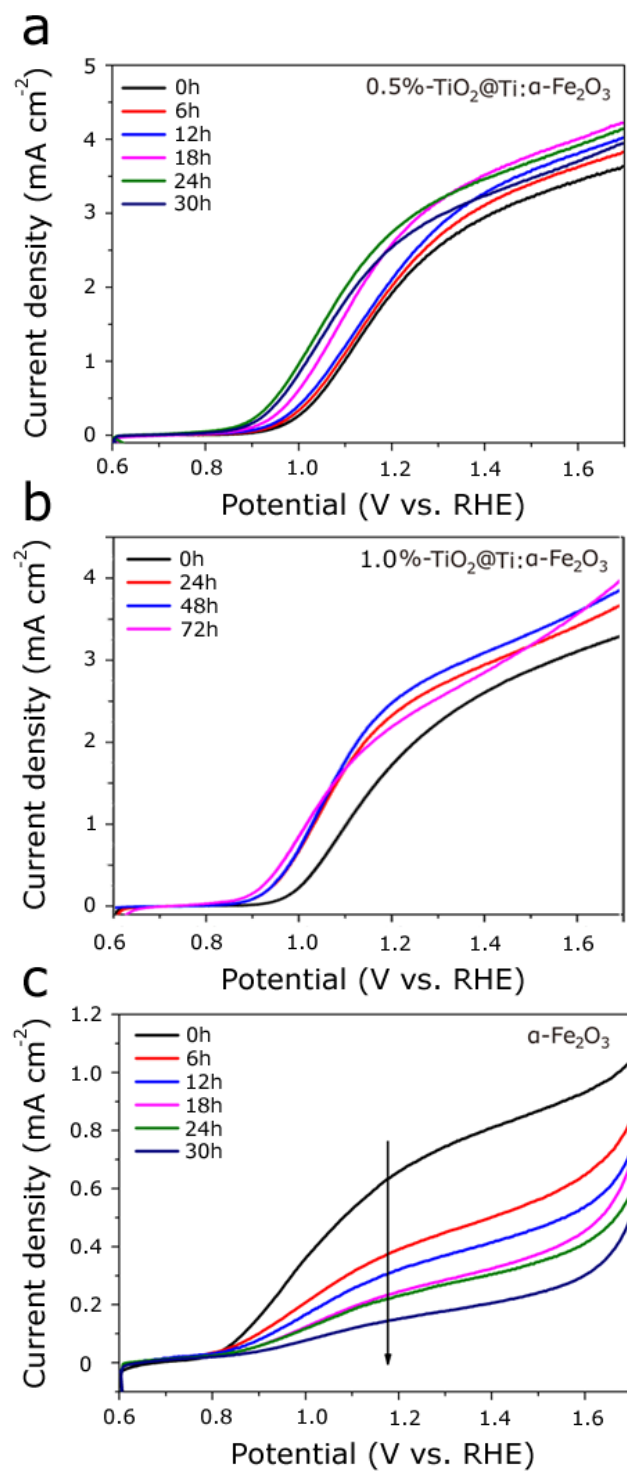


Figure S14. The variation in the PEC performance of the (a) 0.5%- TiO_2 @Ti: α - Fe_2O_3 , (b) 1.0%- TiO_2 @Ti: α - Fe_2O_3 , and (c) α - Fe_2O_3 photoanodes with increasing H_2O_2 soaking time.

H₂O₂ soaking treatment was conducted on the 0.5%-TiO₂@Ti:α-Fe₂O₃, 1.0%-TiO₂@Ti:α-Fe₂O₃, and α-Fe₂O₃ photoanodes, respectively. Their *J*–*V* curves under the illumination of a Xe lamp (Light intensity: ~450 mW cm⁻²) at different H₂O₂ soaking times were recorded in Figure S14. The PEC performance of both the 0.5%-TiO₂@Ti:α-Fe₂O₃ and 1.0%-TiO₂@Ti:α-Fe₂O₃ photoanodes increase first and then decrease with increasing H₂O₂ soaking time, and the optimal soaking time in H₂O₂ solution for them is 24 h and 48 h, respectively (Figure S14a and b), while the photocurrent density of the α-Fe₂O₃ photoanode decreases continuously with the increase of H₂O₂ soaking time (Figure S14c). Hence, the increase in their PEC performance is definitely originated from the removal of hole injection barrier imposed by the TiO₂ encapsulation layer, and the decrease with prolonged H₂O₂ soaking time is also reasonable because the H₂O₂ soaking treatment has an adverse effect on the PEC activity of the hematite pristine photoanode.

The changes in the photocurrent densities of the 0.5%-TiO₂@Ti:α-Fe₂O₃ and 1.0%-TiO₂@Ti:α-Fe₂O₃ with prolonging the H₂O₂ soaking time can be understood by the following mechanism. For short time treatments the TiO₂ layer is still thick enough to separate Fe₂O₃ from H₂O₂ solution, and the current density maintains monotonous increasing behavior with increasing treatment time. For longer treatment time the TiO₂ layer is no longer thick enough to protect the Fe₂O₃ and the interface recombination rate will be affected by the H₂O₂ solution (Figure S14a and b). From Figure S13c we can see that the current density at the pure Fe₂O₃ surface decreases dramatically with longer H₂O₂ treatment. These two mechanisms compete with each other and make a non-monotonic change of the current with increasing H₂O₂ treatment time.

As for the difference in the optimal H₂O₂ soaking time for the 0.5%-TiO₂@Ti:α-Fe₂O₃ and 1.0%-TiO₂@Ti:α-Fe₂O₃ photoanodes, it could be attributed to the different thicknesses of the TiO₂ encapsulation layers on their surfaces. In addition, the photocurrent density of the 1.0%-TiO₂@Ti:α-Fe₂O₃ photoanode after H₂O₂ soaking is lower than that of the Ti:α-Fe₂O₃ photoanode, verifying that a volume fraction of 0.5% is the optimal TiCl₄ concentration in the spin-coated ethanol solution

when preparing hematite photoanode using the dopant-containing layer encapsulation approach.

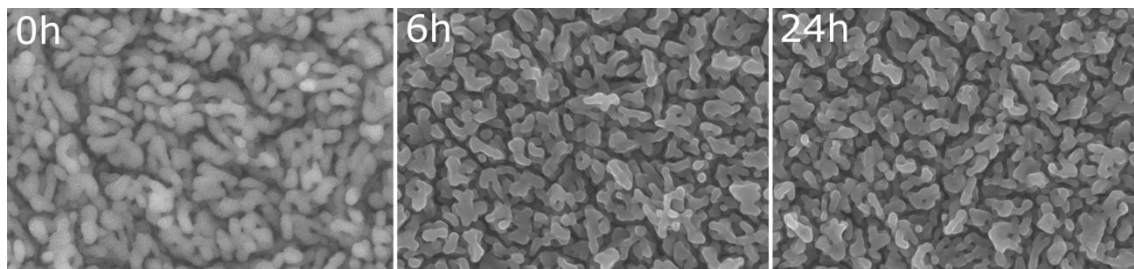


Figure S15. SEM images of the α -Fe₂O₃ photoanodes at different H₂O₂ soaking time.

H₂O₂ soaking treatment for longer time has little influence on the morphology of the α -Fe₂O₃ photoanode, excluding the possibility of the instability of the photoanode material for the deteriorated performance.

Table S2. Comparison of PEC performance of Ti: α -Fe₂O₃ photoanodes.

photoanode	Light source	Photocurrent* (mA/cm ²)	IPCE	Reference
Ti: α -Fe ₂ O ₃ wormlike nanostructure	AM 1.5G, 100 mW/cm ²	0.83	19% @370 nm at 1.23 V vs. RHE	Our work
Ti: α -Fe ₂ O ₃ film	AM 1.5G, 100 mW/cm ²	2.80	24% @350 nm at 1.02 V vs. RHE	7
Ti: α -Fe ₂ O ₃ nanorod array	AM 1.5G, 100 mW/cm ²	2.28	27.3% @350 nm at 1.23 V vs. RHE	8
Ti: α -Fe ₂ O ₃ urchin-like nanostructure	AM 1.5G, 100 mW/cm ²	1.91	60% @350 nm at 1.53 V vs. RHE	9
Ti: α -Fe ₂ O ₃ micro-nano structures	AM 1.5G, 100 mW/cm ²	1.2	Not provide	10
Ti: α -Fe ₂ O ₃ nanorod array	AM 1.5G, 100 mW/cm ²	0.72	Not provide	11
Ti: α -Fe ₂ O ₃ nanowire film	AM 1.5G, 100 mW/cm ²	0.67	Not provide	12
Ti: α -Fe ₂ O ₃ ultrathin film	AM 1.5G, 100 mW/cm ²	~0.5	~11% @350 nm at 1.23 V vs. RHE	13
Ti: α -Fe ₂ O ₃ wormlike nanostructure	AM 1.5G, 100 mW/cm ²	0.2	~5% @360 nm at 1.2 V vs. RHE	14
Ti: α -Fe ₂ O ₃ micro-nano structures	AM 1.5G, 100 mW/cm ²	0.15	Not provide	15

* Photocurrent is obtained at a bias of 1.23 V vs. RHE.

Table S2 lists a literature survey of some recent publications of Ti-doping hematite photoanodes. Although the photocurrent density of our sample is much lower than some reported results, the IPCE value shows a comparable value to the reported ones. We think one of the possible reason for the big difference in photocurrent density is the difference in light source used for the measurements. In fact, it is challenging to compare the measured photocurrent densities reported by different research laboratories given that the irradiance spectrum may vary from different light sources (e.g. lamp lifetime and power) and filter used in the measurements. In this regard, IPCE, which is independent from the specific light source, is a better parameter for comparison.

References

- (1) Moulder, J. F.; Stickle, W. F.; Sobol, P. E.; Bomben, K. *Handbook of X-ray photoelectron spectroscopy*, Physical Electronics Inc.: Eden Prairie, 1992.
- (2) Bandara, J.; Mielczarski, J. A.; Kiwi, J. 1. Molecular mechanism of surface recognition. Azo dyes degradation on Fe, Ti, and Al oxides through metal sulfonate complexes. *Langmuir* **1999**, *15* (22), 7670-7679.
- (3) Kay, A.; Cesar, I.; Grätzel, M. New benchmark for water photooxidation by nanostructured α -Fe₂O₃ films. *J Am Chem Soc* **2006**, *128* (49), 15714-15721.
- (4) Le Formal, F.; Gratzel, M.; Sivula, K. Controlling Photoactivity in Ultrathin Hematite Films for Solar Water-Splitting. *Adv Funct Mater* **2010**, *20* (7), 1099-1107.
- (5) Dotan, H.; Sivula, K.; Gratzel, M.; Rothschild, A.; Warren, S. C. Probing the photoelectrochemical properties of hematite (α -Fe₂O₃) electrodes using hydrogen peroxide as a hole scavenger. *Energ Environ Sci* **2011**, *4* (3), 958-964.
- (6) Klahr, B.; Gimenez, S.; Fabregat-Santiago, F.; Bisquert, J.; Hamann, T. W. Electrochemical and photoelectrochemical investigation of water oxidation with hematite electrodes. *Energ Environ Sci* **2012**, *5* (6), 7626-7636.
- (7) Wang, G.; Ling, Y.; Wheeler, D. A.; George, K. E.; Horsley, K.; Heske, C.; Zhang, J. Z.; Li, Y. Facile synthesis of highly photoactive α -Fe₂O₃-based films for water oxidation. *Nano Lett* **2011**, *11* (8), 3503-3509.

- (8) Wang, D.; Chen, H.; Chang, G.; Lin, X.; Zhang, Y.; Aldalbahi, A.; Peng, C.; Wang, J.; Fan, C. Uniform doping of titanium in hematite nanorods for efficient photoelectrochemical water splitting. *Acs Appl Mater Inter* **2015**, *7* (25), 14072-14078.
- (9) Deng, J.; Zhong, J.; Pu, A.; Zhang, D.; Li, M.; Sun, X.; Lee, S.-T. Ti-doped hematite nanostructures for solar water splitting with high efficiency. *J Appl Phys* **2012**, *112* (8), 084312.
- (10) Miao, C.; Shi, T.; Xu, G.; Ji, S.; Ye, C. Photocurrent enhancement for Ti-doped Fe₂O₃ thin film photoanodes by an in situ solid-state reaction method. *Acs Appl Mater Inter* **2013**, *5* (4), 1310-1316.
- (11) Fu, Z.; Jiang, T.; Liu, Z.; Wang, D.; Wang, L.; Xie, T. Highly photoactive Ti-doped α -Fe₂O₃ nanorod arrays photoanode prepared by a hydrothermal method for photoelectrochemical water splitting. *Electrochim Acta* **2014**, *129*, 358-363.
- (12) Franking, R.; Li, L. S.; Lukowski, M. A.; Meng, F.; Tan, Y. Z.; Hamers, R. J.; Jin, S. Facile post-growth doping of nanostructured hematite photoanodes for enhanced photoelectrochemical water oxidation. *Energ Environ Sci* **2013**, *6* (2), 500-512.
- (13) Ding, D.; Dong, B.; Liang, J.; Zhou, H.; Pang, Y.; Ding, S. Solvothermal-Etching Process Induced Ti-Doped Fe₂O₃ Thin Film with Low Turn-On Voltage for Water Splitting. *Acs Appl Mater Inter* **2016**, *8* (37), 24573-24578.
- (14) Li, Q.; Bian, J.; Zhang, N.; Ng, D. H. Loading Ni(OH)₂ on the Ti-doped hematite photoanode for photoelectrochemical water splitting. *Electrochim Acta* **2015**, *155*, 383-390.
- (15) Miao, C.; Ji, S.; Xu, G.; Liu, G.; Zhang, L.; Ye, C. Micro-nano-structured Fe₂O₃:Ti/ZnFe₂O₄ heterojunction films for water oxidation. *Acs Appl Mater Inter* **2012**, *4* (8), 4428-4433.